ACS APPLIED ENERGY MATERIALS

Article

Cross-Section Auger / XPS imaging of conversion type electrodes: how their morphological evolution controls the performance in Li-ion batteries

Lénaïc Madec, Jean-Bernard Ledeuil, Gaël Coquil, Laure Monconduit, and Hervé Martinez

ACS Appl. Energy Mater., **Just Accepted Manuscript** • DOI: 10.1021/acsaem.9b01115 • Publication Date (Web): 11 Jun 2019

Just Accepted

is published by the American Chemical Society. 1155 Sixteenth Street N.W., Washington, DC 20036

Cross-Section Auger / XPS imaging of conversion type electrodes: how their morphological evolution controls the performance in Li-ion batteries

Lénaïc Madec[†,#,*], Jean-Bernard Ledeuil[†], Gaël Coquil[‡], Laure Monconduit[‡,#] and Hervé Martinez[†,#]

[†] CNRS/ UNIV Pau & Pays Adour/ E2S UPPA, Institut des Sciences Analytiques et de Physicochimie pour l'Environnement et les Matériaux, UMR5254, 64000, Pau, France

[‡] ICG-AIME, Bat 15, cc 15-02, Université Montpellier 2, Pl. E. Bataillon, 34095 Montpellier cedex 5, France

[#] Réseau sur le Stockage Electrochimique de l'Energie (RS2E), CNRS FR3459, 33 Rue Saint Leu, 80039 Amiens Cedex, France

ABSTRACT: Conversion type reaction have revolutionized the field of Li-ion batteries and beyond in term of electrochemical performance and fundamental aspects. However, direct evidence of this reaction over long term cycling, still has to be demonstrated. Indeed, investigating the morphological conversion mechanism at both the electrode and nanometer scales remains very challenging. Here, the use of advanced Auger / µXPS imaging of electrodes cross-sections, prepared by ion-milling, is proposed. Through the study of TiSnSb based electrodes, the role of the inactive element (here Ti) in the long term reversibility of the conversion reaction is highlighted. Importantly, Ti, Sn and Sb are found together at the nanometer scale despite a total spreading over tens of micron which directly proves the electrochemical conversion of the TiSnSb material even after 400 cycles. Moreover, a gradual shell to core expansion/break up of TiSnSb particles is revealed during the continuous conversion reactions and leads to highly porous structures after 400 cycles. This phenomenon, more uniform at 60°C, is at the origin of the higher electrochemical performance at this temperature. Overall, the innovative approach proposed in this work will benefit not only to the study of conversion/alloying based batteries but also to all-solid-state batteries for which buried interfaces have to be reached.

KEYWORDS: Li-ion battery, conversion material, morphological evolution, cross-section, Auger, XPS.

INTRODUCTION

Developing high-energy Li-ion cells for portable electronic devices and electric vehicles is one of the most challenging problems for battery researchers. Beyond the continuous improvement of nickel manganese cobalt (NMC) and nickel cobalt aluminum (NCA) lithiated oxides-based cathodes, developing anodes with superior performance is of great interest to meet the future energy requirement.[1] Conversion and alloying anode materials have thus been extensively studied because of their high theoretical capacity (700-1500 mA h g^{-1}) compared to graphite (372 mA h g^{-1}).[2] These materials suffer, however, from large volume expansion (typically >200%) during lithiation/delithiation, resulting in pulverization of active material, loss of electrical contact[3] and continuous electrolyte degradation due to the solid electrolyte interphase (SEI) breaking and reforming upon cycling.[2] In the case of conversion material, the most successful approach to tackle these issues is more likely the use of composite materials constituted of electrochemically active/inactive elements to buffer the volume change and thus to enhance the electrochemical performance.[2,4] However, the role of the inactive elements in the long term conversion reaction still remains to be elucidated. In that direction, innovative analytical approaches allow investigating the Li-storage mechanism of conversion/alloying anode materials at the nanoscale.[5]

Among these approaches, e*x situ* transmission electron spectroscopy (TEM) have been widely used to study conversion materials at the nanoscale. In particular, it allowed to confirm the reduction of metal oxides through the formation of metal nanograins dispersed in a Li_2O matrix[6,7,8] as initially suggested by X-ray diffraction.[9] Similarly, high-resolution TEM coupled to electron energy-loss spectroscopy (EELS) was used to study the conversion mechanism of metal fluorides.[10] FeF_2 was found to form a continuous Fe network dispersed in a LiF matrix while CuF_2 formed segregated Cu particles, thus explaining the much higher reversibility of the FeF_2 conversion process.

More recently, *in situ*/*in operando* techniques have been developed to provide direct observation of volume variations, strain changes and surface film formation occurring at the nanoscale during the

lithiation/delithiation processes of conversion and alloying materials. In particular, *in situ* TEM allows to study the lithiation/delithiation of individual nanostructures (i.e. nanowire or nanoparticles) with near-atomic resolution in real time.[11] Some caution should, however, be taken as this technique focuses on the analysis of individual nanostructures for which the electronic and ionic connection is commonly realized through a single contact point so that their lithiation/delithiation mechanism can be strongly influenced. As a matter of fact, *in situ* TEM revealed that pure CoS_2 particles convert through an anisotropic process with cracks formation while CoS_2 particles anchored on reduced graphene oxide sheets (i.e. well electronically connected) convert through a core-shell process with almost no cracks.[12] Therefore, such individual nanostructures studies may not be representative of the reactivity occurring in three-dimensional electrodes. To overcome this issue, *in operando* X-ray tomographic microscopy (SRXTM) has been proposed to simultaneously visualize in three-dimension both chemical composition and morphology changes occurring at both individual particles and electrode level.[13] It allowed to reveal a core-shell lithiation of SnO particles with some cracks initiation along pre-existing defects followed by a partial particle densification during delithiation along with irreversible distortion of the electrode.[13]

Surface characterization techniques such as Auger electron spectroscopy (AES) and time of flight secondary ion mass spectrometry (ToF-SIMS) have also been used as alternative approaches to study conversion/alloying mechanisms at the nanoscale. In that case, depth profiling or cross-section analysis are mandatory to probe the particles/electrodes volume properties. For instance, the high spatial resolution of AES coupled to depth profiling allowed to confirmed the core-shell lithiation process of Si particles (5 µm) with respect to their electrode environment.[14] Similarly, ToF-SIMS and AES performed on Si-based electrode cross-section prepared by focused ion beam (FIB) revealed an homogeneous core-shell mechanism of Si particles along the electrode thickness as well as a progressive lithium trapping in Si particles upon cycling.[15] Moreover, AES depth profiling,[16] *in situ* AES[17,18] and cross-section AES[19] have been used to characterize the morphology and composition of solid electrolyte interphases (SEI) formed at the surface of various Li-ion anode and cathode materials. Note that AES was also used to study cross-section of Li/LiPON/$LiCoO_2$ solid state micro-batteries[20] as well as cross-section of Ag/Au@SiO_2 core-shell nanoparticles with a high resolution (~12 nm).[21] Additional techniques such as electron probe microanalysis (EPMA) and scanning spreading resistance microscopy (SSRM) have also been used to study cross-section of Si-C/graphite electrodes after long term cycling (300 cycles) and showed that Si-C particles severely degrade with a loss of electronic conductivity while graphite particles barely change.[22]

Among conversion materials for negative electrodes, TiSnSb was recently proposed[23] with improved performance using CMC as binder[24] and FEC and VC as electrolyte additives.[25] More recently, TiSnSb showed unexpected superior lifetime, CE and polarization at 60°C compared to 25°C.[26] This was explained by a specific reactivity of the electrolyte used (1M $LiPF_6$ EC:PC:3DMC +5% FEC + 1% VC) at 60°C that forms a more stable/passivating SEI film with only a partial electrolyte additives consumption as observed by X-ray photoelectron spectroscopy (XPS) and gas chromatography coupled with electron impact mass spectrometry (GC/MS), respectively. Considering the TiSnSb conversion process, Li_3Sb and Li_7Sn_2 phases were first reported to form after full lithiation using X-ray diffraction (XRD)[23] which was then confirmed by X-ray absorption spectroscopy (XAS).[27] Interestingly, the charge process was revealed only recently thanks to operando XAS analysis that showed the formation of a "Ti-Sn-Sb like" compound after full delithiation with distinct and amorphous structural properties compared to pristine TiSnSb.[27] This spectroscopic study thus confirmed a reversible conversion reaction. Nonetheless, the role of the Ti and the morphological evolution of TiSnSb particles at the nanometer and electrode scales during long term cycling remains unclear so far.

This study therefore aims at revealing the morphological conversion mechanism at both the electrode and nanometer scales over long term cycling. To do so, advanced Auger electron spectroscopy (AES) / scanning Auger microscopy (SAM) and µXPS parallel imaging were used to investigate TiSnSb based electrodes cross-sections prepared by ion-milling.

EXPERIMENTAL

Materials and methods used for TiSnSb synthesis and electrodes preparation are fully described in our previous study.[26] For clarity, the electrode composition was 70:9:9:12 weight ratio of TiSnSb:carbon black:VGCF:CMC and the TiSnSb loading was 3 mg cm-2 ±0.3 mg. The electrolyte was 1M LiPF6 EC:PC:3DMC + 5% FEC + 1% VC. Cycling at either 25°C or 60°C was performed between 0.02-1.5 V as followed: a first cycle at C/2 rate (i.e. 0.5 mole of Li per mole of TiSnSb per hour) with a 48 h storage period at 0.02 V followed by 400 cycles at 4C, stopped in charge. After cells opening, separators and TiSnSb electrodes were used for GC/MS and surface analysis, respectively. Corresponding analysis conditions can be found in details in our previous study.[26] Before surface analysis, TiSnSb electrodes were washed twice by immersion in DMC (anhydrous, ≥99% purity, Aldrich, 1 ml) in a clean and dry glass vial with a mild manual agitation (10s). Importantly, all surface analysis of TiSnSb electrodes (including cross-section analysis) were performed after long term cycling (400 cycles) on the same electrodes.

Electrode cross-section preparation by ion-milling. TiSnSb cross-sectioned electrodes were prepared using a JEOL Cross-Polisher (JEOL Ltd, Tokyo, Japan) in a nitrogen-filled glove box. Electrodes were first sandwiched between two silicon wafers using a silver conducting epoxy resin. Then at 1.10^{-4} Pa, the resulting assemblies were exposed at normal angle to the Ar^+ ion beam working at 6

keV (i.e. ion current of ~120 µA) for 8h. This method allows obtaining perfect planar surface as seen in Figure S1. Note that ion milling performed at normal angle leads to almost no Ar^+ ions implantation (here, Ar LMM Auger lines were not observed in the survey spectra at 211 and 195 eV KE) so that resulting sample damage would be limited to amorphization phenomenon with the same chemical composition. Moreover, the usual perturbation observed with ion milling cross-section is material re-deposition due to the sputtering process, which could lead to curtaining process. More information can be found in the literature.[28,29,30]

Scanning electron microscopy (SEM), Auger electron spectroscopy (AES) and scanning Auger microscopy (SAM). Note first that the Auger spatial resolution is about 10-20 nm with a probing depth of about 2-3 nm in the analysis conditions used. SEM, AES and SAM were performed using a JEOL JAMP 9500 F Auger spectrometer (JEOL Ltd, Tokyo, Japan) equipped with a Schottky Field Emission gun and a hemi-spherical analyser coupled with a high dynamic multichannel detector. The typical operating pressure was <2 x10-7 Pa. Note that the thickness of cross-sectioned electrodes was measured by SEM at 0° tilt (not shown) while other analysis were performed at 30-40° tilt to prevent charging effect. The electron kinetic energy were recorded using either: (i) CAE mode (constant analyzer energy, also called FAT or CAR mode) corresponding to a fixed energy resolution (dE=constant) or (ii) CRR mode (constant relative resolution, also called FRR mode) corresponding to a relative energy resolution (dE/E=constant). AES survey spectra were recorded between 15 to 2000 eV with 1 eV step size using a focused probe and a CRR mode with dE/E = 0.5% (high sensitivity). In the different Figures, Auger spectra are presented using the EN(E) mode expressed as the output signal of the electron detector using "true" pulse counting versus kinetic energy. Note that in some spectra, a low intensity peak was observed at ~100 eV and is attributed to a slight silicon deposition from the Si wafer during ion-milling. SAM (elemental 2D distribution) images were recorded using a CAE mode to enable defining the useful energy width needed to obtain a significant peak to background-intensity difference with respect to the Auger transition and the backgrounds shape. Note that each SAM image is represented using "peak minus background" (P-B) Auger intensity for a transition (ΔE/E=0.5%). Also, SAM overlays interpretation usually need AES spectra carried out at particular position to confirm the composition or particular bounding. An "auto probe tracking" correction was also applied to control and compensate any potential drift (i.e. sample surface charge effects, vibration, electronic and electromagnetic field variations, sample heat dissipation, etc.) during acquisition.

X-ray photoelectron spectroscopy. Note first that the XPS probing depth is about 5-7 nm. XPS analysis was performed using an Escalab 250 Xi spectrometer with a monochromatized Al Kα radiation (hv=1486.6 eV). Samples were put on a sample holder using an insulating uPVC tape (reference 655 from 3 M) then the samples transfer was performed through an argon-filled glove box directly connected to the spectrometer. Analysis was performed using the standard charge compensation mode and an elliptic 325×650 µm X-ray beam spot.

Classical electrodes surface XPS analysis was performed by recording core spectra with a 20 eV constant pass energy, 0.15 eV step size and short time iterative scans. Quantification was performed using CasaXPS software. Core peaks were calibrated from the 285 eV peak (C-C/C-H) while the fitting was performed using non-linear Shirley-type background with 70% Gaussian - 30% Lorentzian Voigt peak shapes, full width at half-maximum constraint range while quantification was done using the relative sensitivity factor provided with the Escalab machine.

XPS parallel imaging was performed on the TiSnSb electrode after 400 cycles at 25°C and cross-section preparation. Core spectra were recorded using a 100 eV constant pass energy (PE) with a 0.8 eV step size in 50 µm small area lens mode (i.e. aperture selected area). Parallel images were recorded using a 400 eV PE in 150 µm image lens mode using a fixed energy for each element. Prior to analysis, both SEM and XPS parallel images (using 500 µm image lens mode) of the electrode cross-section were used to precisely select areas of interest.

RESULTS AND DISCUSSION

Figure 1a summarizes the long-term electrochemical performance of TiSnSb electrodes performed at 4C rate and 25°C or 60°C as well as the main GC/MS and XPS results obtained after 400 cycles. Overall, much higher capacity retention and coulombic efficiency (*CE*) as well as lower polarization was observed at 60 °C compared to 25°C. These results are therefore unexpected considering the poorer performance and shorter lifetime normally observed for high temperature Li-ion cells.[31,32,33] Although kinetic effects could partially explain both the lower polarization / higher capacity retention at 60°C, it cannot explain the higher *CE*. Interestingly, GC/MS analysis (Figure 1b) showed a much lower electrolyte degradation at 60°C (*i.e.* only a partial additives consumption) compared to 25°C (*i.e.* full additives consumption and further EC degradation). It therefore suggests the formation of a more stable/passivating SEI film at the TiSnSb electrode surface at 60°C, in good agreement with the higher *CE*. For information, cycling at 60°C led to a much higher LiF content (30 at.%) compared to 25°C (4 at.%), highlighting a larger $LiPF_6$ degradation (Figure 1c). A much higher Li_2CO_3 content (50 at.%) was, however, observed at 25°C compared to 60°C (20 at.%), more likely due to the higher solvent degradation. To get more insights on the morphological conversion mechanism at both the electrode and nanometer scales, cross-sections of a pristine TiSnSb electrode and electrodes after 400 cycles at 25°C and 60°C were then prepared by ion-milling and analysed using advanced Auger / µXPS parallel imaging.

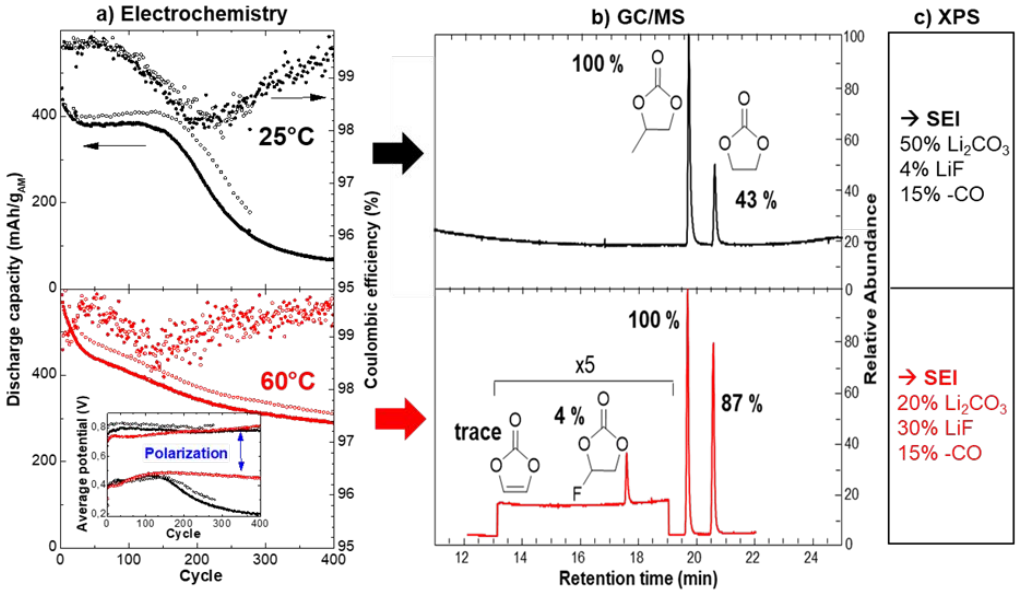

Figure 1. a) Discharge capacity, coulombic efficiency and polarization (inset) versus cycle number of TiSnSb/Li coin cells cycled at 25°C or 60°C in 1M LiPF6 EC:PC:3DMC + 5% FEC + 1% VC between 0.02-1.5 V at 4C (i.e. 4 mole of Li per mole of TiSnSb per hour). b) Chromatograms of the electrolyte (The relative abundance of each peak was normalized relatively to PC) and c) Main SEI species at the TiSnSb electrodes surface (in at.%, from XPS quantification) as extracted for the same TiSnSb/Li coin cells after 400 cycles. For clarity, reference [26] fully described the XPS and GC/MS analysis conditions and also present the full XPS quantification table with peak assignments.

SEM, AES and SAM of the pristine TiSnSb electrode cross-section. Figure 2a shows a SEM image of a pristine (uncycled) TiSnSb electrode cross-section. The Cu current collector and the silver epoxy resin were observed at the bottom and on top of the composite electrode, respectively. The electrode of 12 ±2 µm thick was constituted of dense and shapeless TiSnSb particles of 0.5-5 µm surrounded by large and porous areas containing the carbon additives and the CMC binder as confirmed by AES spectra (Figure 2b). Indeed, carbons/CMC areas showed intense C KLL transitions (150-270 eV KE) and weak O KLL transitions (470-510 eV KE) while TiSnSb particles showed the expected Ti LMM (350-400 eV KE), Sn MNN (400-440 eV KE) and Sb MNN (440-470 eV KE) transitions. Interestingly, O KLL peaks were also observed on TiSnSb particles more likely due to the formation of small amount of oxide phases during the TiSnSb synthesis. As a matter of fact, Sn and Sb oxides were previously observed at the pristine electrode surface by XPS while the as prepared powder diffractogram was unequivocally assigned to TiSnSb.[26] Note that a low intensity C KLL peak was also observed on TiSnSb particles due to possible low contamination of the flat surface before analysis. The SAM images then clearly confirm that dense TiSnSb particles were surrounded by carbons areas (Figure 2c) and show a perfect overlay of the Ti, Sn and Sb elements (Figure 2d).

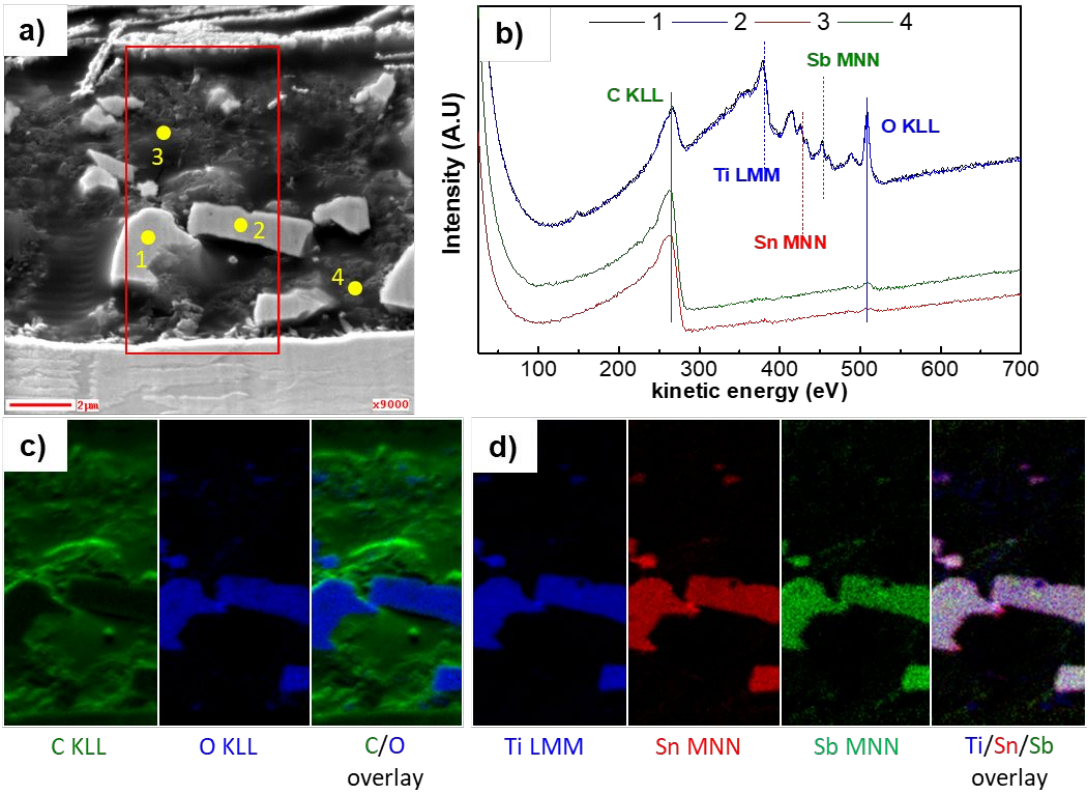

Figure 2. a) SEM image of a pristine TiSnSb electrode cross-section, b) Auger spectra taken at different position as indicated in the SEM image. SAM (elemental 2D distribution) images of c) C KLL, O KLL transitions and their overlay and d) Ti LMM, Sn MNN, Sb MNN transitions and their overlay. The area at which the SAM images were taken is indicated in the SEM image.

SEM, AES and SAM of TiSnSb electrodes cross-section after 400 cycles at 25°C and 60°C. Figure 3a shows a SEM image of a 25°C cycled TiSnSb electrode cross-section. The thickness of the electrode was 50 ±3 µm compared to 12 ±2 µm for the pristine electrode, which indicates a large volume expansion upon the long term cycling. This can be explained by the significant morphology change of the TiSnSb particles. Indeed, while dense particles were still observed, they were now surrounded by the formation of non-uniform porous shell. This was confirmed by AES spectra for which Ti LMM, Sn MNN and Sb MNN peaks were detected (Figure 3b). Note also that dense cores showed some cracks. These results are explained by a non-uniform shell to core expansion/break up of TiSnSb particles over long term cycling. Consequently, the spreading/pulverization of TiSnSb particles led to the electrode porosity filling as well as to an increase of the electrode thickness. SAM images further confirmed the formation of a dense core-porous shell structure of the TiSnSb particles (Figure 3d). Importantly, this result represents a direct proof of the conversion type reaction of this electrode material even after 400 cycles. However, some discrepancies of the Ti, Sn and Sb elements distribution over the porous shells were observed which indicates a non-uniform spreading of the different elements/phases during the continuous conversion reactions. Interestingly, the SAM images of C, O, and their overlay showed that carbon areas contain almost no oxygen (Figure 3c). The overlay of C, O and Ti showed, however, that oxygen areas mostly overlapped the porous TiSnSb areas while no oxygen was observed on the dense TiSnSb areas (Figure 3f). These results suggest the formation of O-containing SEI species inside the TiSnSb porous shell structure due to the continuous electrolyte degradation at the fresh TiSnSb surface formed by the expansion/break up of particles over long term cycling. Similarly, the SAM images of F KLL and its overlay with C and O elements showed that F-based species (formed by $LiPF_6$ degradation) overlapped well with the oxygen areas, *i.e.* inside the TiSnSb porous shell structure (Figure 3e). Figure 4a shows a SEM image of a 60°C cycled TiSnSb electrode cross-section. Note the absence of current collector for this sample due to a complete but clean delamination of the electrode during the assembly between the silicon wafers. For clarity, the current collector was located at the top of the electrode so that silver epoxy resin was observed instead. The thickness of the electrode was 65 ±3 µm compared to 50 ±3 µm for the 25°C cycled electrode, which indicates a larger volume expansion upon the long term cycling at 60°C. This is in agreement with the further morphology change of the TiSnSb particles. Indeed, highly porous and large TiSnSb structures (with nearly no dense areas) were surrounded by carbons/CMC areas (Figure 4a) as confirmed by AES spectra (Figure 4b) and SAM images (Figure 4c-f). This is explained by the much higher capacity retention during the 60°C cycling that led to a higher expansion/break up of TiSnSb particles, compared to 25°C. Therefore, the spreading/pulverization of TiSnSb particles clearly leads to both the electrode porosity filling and the electrode

thickness increase. Surprisingly, however, no discrepancy of the Ti, Sn and Sb elements distribution was observed over the porous structure (Figure 4d). This indicates a uniform spreading of the different elements/phases during the continuous conversion reactions compared to 25°C. As a matter of fact, the presence of Ti LMM, Sn MNN, Sb MNN transitions on the AES spectra (whatever the analysis position was) further confirmed the presence of Ti, Sn and Sb at the nanometer scale. Indeed, the analysis spot size is about 10-20 nm. This result is of great importance as it proves the continuous reformation of a TiSnSb-like phase over 400 cycles which is even more surprising considering a total spreading over tens of micron. Interestingly also, both oxygen and fluorine areas overlapped well the porous TiSnSb areas (Figure 4e-f), similarly to 25°C. It therefore confirms that SEI species are mostly formed inside the porous TiSnSb structure due to the electrolyte degradation at the fresh surface formed by the continuous expansion/break up of particles over long term cycling.

Overall, the continuous conversion reactions greatly affect the TiSnSb morphology. It changes from dense TiSnSb particles to highly and large porous structures. At this point, to confirm that such morphological evolution does not occur as soon as the first lithiation, a TiSnSb electrode cross-section was analyzed after the first discharge at 25°C (Figure S2). It was found that TiSnSb particles indeed remained dense with only few cracks while their homogeneous lithiation was confirmed by AES spectra and SAM images of the lithium. Moreover, the electrode thickness was 16 ±2 µm compared to 12 ±2 µm for the pristine electrode, which indicates that the porosity of the CMC based electrode greatly helps to absorb the volume expansion during the conversion reaction of TiSnSb into $Li_3Sb/Li_7Sn_2/Ti$.

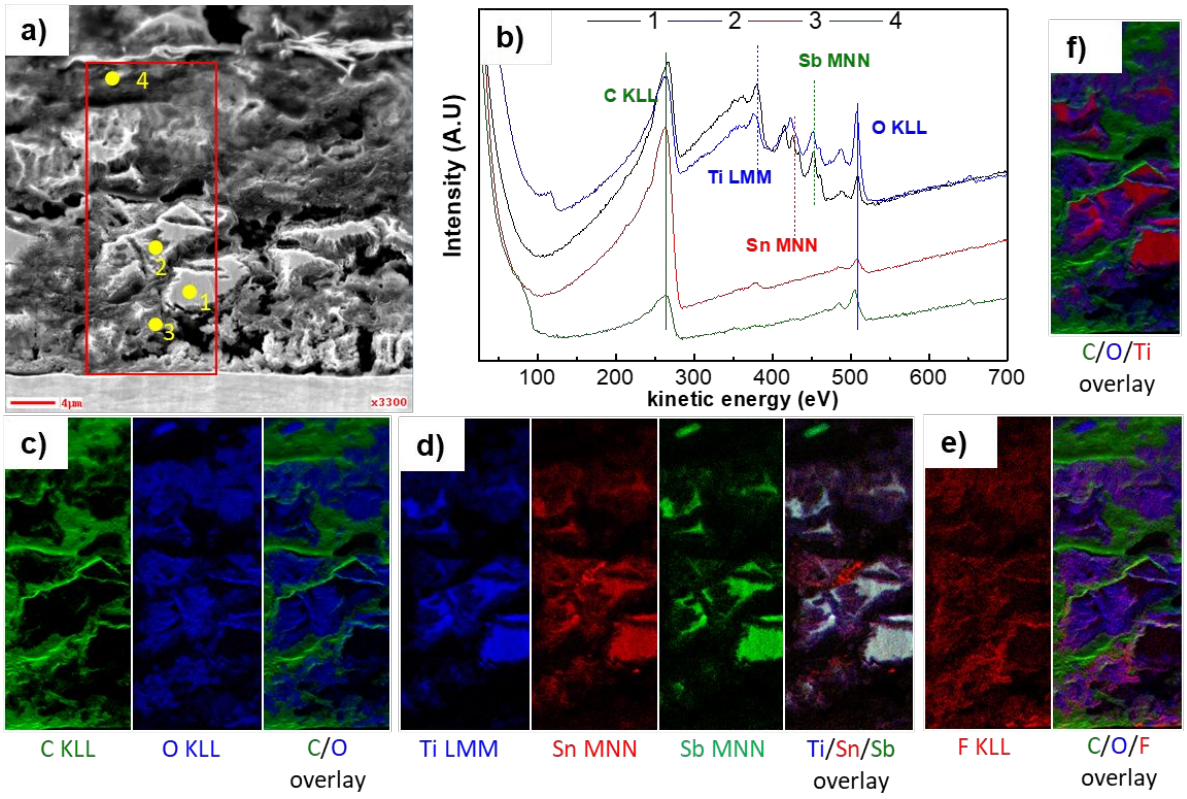

Figure 3. a) SEM image of a TiSnSb electrode cross-section at the end of charge after 400 cycles at 25°C, b) Auger spectra taken at different position as indicated in the SEM image. SAM (elemental 2D distribution) images of c) C KLL, O KLL transitions and their overlay, d) Ti LMM, Sn MNN, Sb MNN transitions and their overlay, e) F KLL transition and C KLL / O KLL / F KLL overlay and f) C KLL / O KLL / Ti LMM overlay. The area at which the SAM images were taken is indicated in the SEM image.

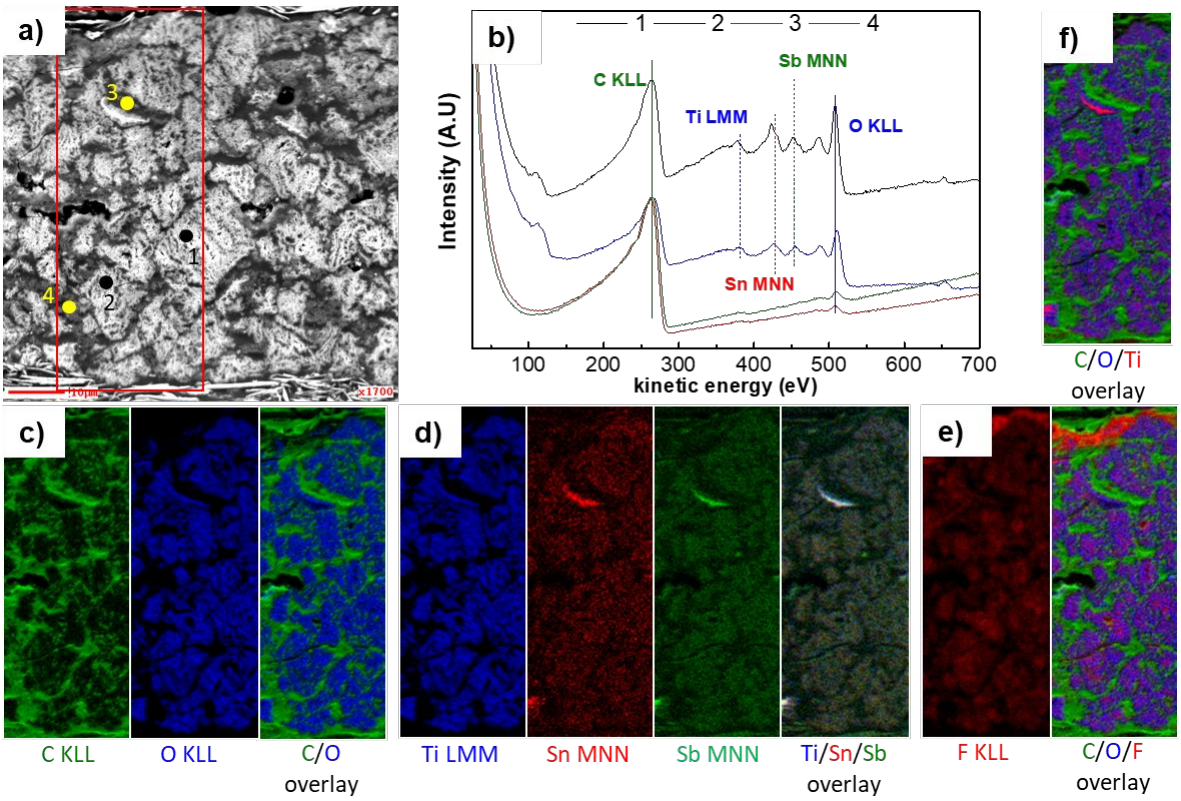

Figure 4. a) SEM image of a TiSnSb electrode cross-section at the end of charge after 400 cycles at 60°C, b) Auger spectra taken at different position as indicated in the SEM image. SAM (elemental 2D distribution) images of c) C KLL, O KLL transitions and their overlay, d) Ti LMM, Sn MNN, Sb MNN transitions and their overlay, e) F KLL transition and C KLL / O KLL / F KLL overlay and f) C KLL / O KLL / Ti LMM overlay. The area at which the SAM images were taken is indicated in the SEM image.

XPS parallel imaging of a TiSnSb electrode cross-section after 400 cycles at 25°C. The aim of this study was to assess the feasibility of µXPS analysis considering the micrometer scale of both TiSnSb particles and TiSnSb/carbons distribution of the electrodes cross-section. Figure 5a shows a SEM image of a TiSnSb electrode cross-section after 400 cycles at 25°C while Figure 5b shows the corresponding high-resolution µXPS parallel image overlay of O 1s (532 eV), Ti 2p (486 eV), Cu 2p (932 eV) and Ag 3d (368 eV). Interestingly, all components of the cross-section (*i.e.* the silver epoxy resin, Cu current collector and electrode) were clearly distinguished in the µXPS parallel image overlay when compare to the SEM image. Moreover, oxygen areas were only partially overlapped by titanium areas as previously observed by Auger (Figure 3). Note that carbon was observed on the whole analysis surface area due to a possible contamination. However, the black areas of the electrode contained neither O nor Ti so they are attributed to the carbon additives areas, in agreement with the SEM/Auger analysis (Figure 3). The presence of O 1s, Ti 2p, Cu 2p and C 1s and was further confirmed by the µXPS core spectra taken at the electrode cross-section scale (Figure 5c). Overall, this study highlights that µXPS parallel imaging can be performed on such unusual samples. In the future, comparison of chemical composition mapping for both electrode surface and cross-section will be considered. However, it will required further optimization to obtain high-resolution core spectra with suitable count rates. Indeed, here, the elements of interest (*i.e.* Ti, Sn, O...) had relatively low counts rates with the settings used. Therefore, µXPS parallel images were recorded using a given energy (*i.e.* peak – background intensity) for each element, which corresponded to an analysis time of about 8h per element. It would thus be quite time consuming to acquire µXPS parallel images using an energy range for each element instead.

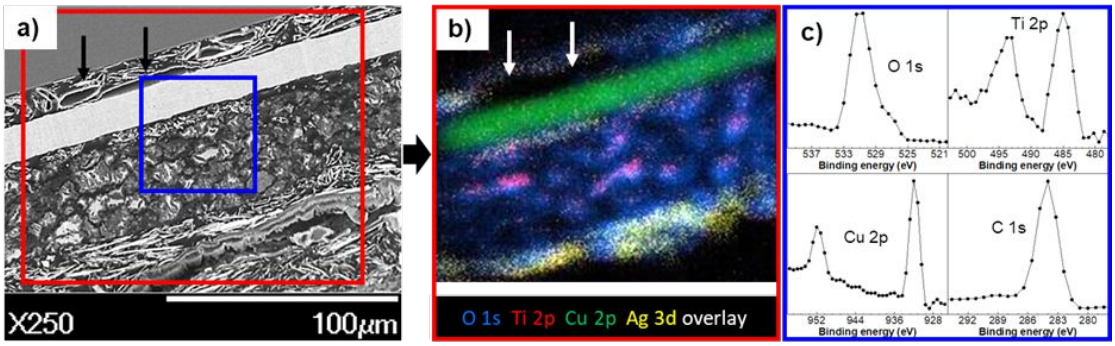

Figure 5. a) SEM image of a TiSnSb electrode cross-section at the end of charge after 400 cycles at 25°C, b) high-resolution parallel XPS image overlay of O 1s, Ti 2p, Cu 2p and Ag 3d for the same TiSnSb electrode cross-section and c), μXPS core spectra of O 1s, Ti 2p, Cu 2p and C 1s (no energy calibration was performed). The areas at which the parallel XPS image and the μXPS core spectra were taken are indicated in the SEM image.

CONCLUSIONS

In this study, the morphological conversion mechanism of TiSnSb over long term cycling was revealed at both the electrode and nanometer scales using cross-section Auger mapping. After the first discharge, TiSnSb particles remained dense (as the pristine ones) and homogeneously lithiated over the electrode thickness while the electrode porosity advantageously buffered the volume expansion of the TiSnSb conversion into $Li_3Sb/Li_7Sn_2/Ti$. During long term cycling (400 cycles), a continuous shell to core expansion/break up of TiSnSb particles occurred so that large highly porous structures were formed. Interestingly, this phenomenon was more uniform at 60°C than 25°C, which can partially explain the better electrochemical performance observed at high temperature. The electrode porosity was thus gradually filled by both the spreading of the porous TiSnSb structures as well as the SEI formed inside these structures so that the electrode thickness increased. More importantly, the presence of Ti, Sn and Sb elements at the nanometer scale despite a total spreading over tens of micron therefore proved the permanent reformation of a TiSnSb-like phase over 400 cycles, which is clearly surprising for such conversion type material.

Interestingly, μXPS parallel imaging was further evaluated to confirm the Auger analysis and opens the possibility to compare the SEI chemical distribution at both electrode surface and cross-section. In that direction, ToF-SIMS coupled to ion etching/in situ FIB depth profiling could also be considered. Furthermore, in the future, X-ray tomography and atomic force microscopy will also be of great interest to probe the 3D morphological and electronic network properties of long term cycling conversion/alloying electrodes for Li-ion battery and beyond. Overall, the innovative approach proposed in this work will benefit not only to the study of all conversion/alloying based batteries but also to all-solid-state batteries for which buried interfaces have to be reached.

ASSOCIATED CONTENT

Supporting Information. Typical SEM images of a TiSnSb electrode cross-section at different magnification ; SEM image and Auger mapping/spectra of a TiSnSb electrode cross-section after the first discharged at 25°C. "This material is available free of charge via the Internet at http://pubs.acs.org."

AUTHOR INFORMATION

Corresponding Author

* E-mail: lenaic.madec@univ-pau.fr

ACKNOWLEDGMENT
This research was performed in the framework of "Réseau sur le Stockage Electrochimique de l'Energie" (RS2E) and the ANR program no. ANR-10-LABX-76-01. Authors thank Total S.A. and ADEME for the financial support of G. Coquil's PhD Thesis and the fruitful discussions.

REFERENCES

(1) Andre, D.; Kim, S.-J.; Lamp, P.; Lux, S. F.; Maglia, F.; Paschos, O.; Stiaszny, B. Future Generations of Cathode Materials: An Automotive Industry Perspective. *J. Mater. Chem. A* **2015**, *3* (13), 6709–6732.

(2) Aravindan, V.; Lee, Y. S.; Madhavi, S. Research Progress on Negative Electrodes for Practical Li-Ion Batteries: Beyond Carbonaceous Anodes. *Adv. Energy Mater.* **2015**, *5*, 1402225.

(3) Beaulieu, L. Y.; Eberman, K. W.; Turner, R. L.; Krause, L. J.; Dahn, J. R. Colossal Reversible Volume Changes in Lithium Alloys. *Electrochem. Solid-State Lett.* **2001**, *4* (9), A137–A140.

(4) Mukhopadhyay, A.; Sheldon, B. W. Deformation and Stress in Electrode Materials for Li-Ion Batteries. *Prog. Mater. Sci.* **2014**, *63* (February), 58–116.

(5) Cui, Q.; Zhong, Y.; Pan, L.; Zhang, H.; Yang, Y.; Liu, D.; Teng, F.; Bando, Y.; Yao, J.; Wang, X.

Recent Advances in Designing High-Capacity Anode Nanomaterials for Li-Ion Batteries and Their Atomic-Scale Storage Mechanism Studies. *Adv. Sci.* **2018**, *5*, 1700902.

(6) Grugeon, S.; Laruelle, S.; Herrera-Urbina, R.; Dupont, L.; Poizot, P.; Tarascon, J.-M. Particle Size Effects on the Electrochemical Performance of Copper Oxides toward Lithium. *J. Electrochem. Soc.* **2001**, *148* (4), A285.

(7) Tarascon, J.-M.; Grugeon, S.; Morcrette, M.; Laruelle, S.; Rozier, P.; Poizot, P. New Concepts for the Search of Better Electrode Materials for Rechargeable Lithium Batteries. *Comptes Rendus Chim.* **2005**, *8* (1), 9–15.

(8) Yonekura, D.; Iwama, E.; Ota, N.; Muramatsu, M.; Saito, M.; Orikasa, Y.; Naoi, W.; Naoi, K. Progress of the Conversion Reaction of Mn3O4particles as a Function of the Depth of Discharge. *Phys. Chem. Chem. Phys.* **2014**, *16* (13), 6027–6032.

(9) Ikeda, H.; Narukawa, S. Behaviour of Various Cathode Materials for Non-Aqueous Lithium Cells. *J. Power Sources* **1983**, *9* (3), 329–334.

(10) Wang, F.; Robert, R.; Chernova, N. A.; Pereira, N.; Omenya, F.; Badway, F.; Hua, X.; Ruotolo, M.; Zhang, R.; Wu, L.; Volkov, V.; Su, D.; Key, B.; Stanley Whittingham, M.; Grey, C. P.; Amatucci, G. G.; Zhu, Y.; Graetz, J. Conversion Reaction Mechanisms in Lithium Ion Batteries: Study of the Binary Metal Fluoride Electrodes. *J. Am. Chem. Soc.* **2011**, *133* (46), 18828–18836.

(11) Liu, N.; Lu, Z.; Zhao, J.; Mcdowell, M. T.; Lee, H. W.; Zhao, W.; Cui, Y. A Pomegranate-Inspired Nanoscale Design for Large-Volume-Change Lithium Battery Anodes. *Nat. Nanotechnol.* **2014**, *9* (3), 187–192.

(12) Su, Q.; Xie, J.; Zhang, J.; Zhong, Y.; Du, G.; Xu, B. In Situ Transmission Electron Microscopy Observation of Electrochemical Behavior of CoS ₂ in Lithium-Ion Battery. *ACS Appl. Mater. Interfaces* **2014**, *6* (4), 3016–3022.

(13) Ebner, M.; Marone, F.; Stampanoni, M.; Wood, V. Visualization and Quantification of Electrochemical and Mechanical Degradation in Li Ion Batteries. *Science (80-.).* **2013**, *342*, 716–720.

(14) Radvanyi, E.; Vito, E. De; Porcher, W.; Danet, J.; Desbois, P.; Larbi, S.; Colin, J. Study of Lithiation Mechanisms in Silicon Electrodes by Auger Electron Spectroscopy. *J. Mater. Chem. A* **2013**, *1* (16), 4956–4965.

(15) Bordes, A.; Vito, E. De; Haon, C.; Boulineau, A.; Montani, A.; Marcus, P.; Bordes, A.; Vito, E. De; Haon, C.; Boulineau, A.; Montani, A. Multiscale Investigation of Silicon Anode Li Insertion Mechanisms by ToF-SIMS Imaging Performed on In Situ FIB Cross Section Multiscale Investigation of Silicon Anode Li Insertion Mechanisms by ToF-SIMS Imaging Performed on I N Situ FIB Cross Section. *Chem. Mater.* **2016**, *28*, 1566–1573.

(16) Kalaga, K.; Shkrob, I. A.; Haasch, R. T.; Peebles, C.; Baren, J.; Abraham, D. P. Auger Electrons as Probes for Composite Micro- and Nanostructured Materials: Application to Solid Electrolyte Interphases in Graphite and Silicon-Graphite Electrodes. *J. Phys. Chem. C* **2017**, *121*, 23333–23346.

(17) Tang, C.; Haasch, R. T.; Ouyang, J.; Dillon, S. J. Insights into Solid-Electrolyte Interphase Induced Li-Ion Degradation from in Situ Auger Electron Spectroscopy. *J. Phys. Chem. Lett.* **2017**, *8*, 6226–6230.

(18) Tang, C.; Leung, K.; Haasch, R. T.; Dillon, S. J. LiMn2O4 Surface Chemistry Evolution during Cycling Revealed by in Situ Auger Electron Spectroscopy and X-Ray Photoelectron Spectroscopy. *ACS Appl. Mater. Interfaces* **2017**, *9*, 33968–33978.

(19) Auvergniot, J.; Cassel, A.; Ledeuil, J.; Viallet, V.; Seznec, V.; Dedryvère, R. Interface Stability of Argyrodite Li6PS5Cl toward LiCoO2, LiNi1/3Co1/3Mn1/3O2, and LiMn2O4 in Bulk All-Solid-State Batteries. *Chem. Mater.* **2017**, *29*, 3883–3890.

(20) Uhart, A.; Ledeuil, J. B.; Pecquenard, B.; Le Cras, F.; Proust, M.; Martinez, H. Nanoscale Chemical Characterization of Solid-State Microbattery Stacks by Means of Auger Spectroscopy and Ion-Milling Cross Section Preparation. *ACS Appl. Mater. Interfaces* **2017**, *9* (38), 33238–33249.

(21) Ledeuil, J.; Uhart, A.; Soulé, S.; Allouche, J.; Dupin, J.-C.; Martinez, H. New Insights into Micro/nanoscale Combined Probes (nanoAuger, mXPS) to Characterize Ag/ Au@SiO2 Core–shell Assemblies. *Nanoscale* **2014**, *6*, 11130–11140.

(22) Kim, S. H.; Kim, Y. S.; Baek, W. J.; Heo, S.; Yun, D.; Han, S.; Jung, H. Nanoscale Electrical Degradation of Silicon–Carbon Composite Anode Materials for Lithium-Ion Batteries. *ACS Appl. Mater. Interfaces* **2018**, *10*, 24549–24553.

(23) Sougrati, M. T.; Fullenwarth, J.; Debenedetti, a.; Fraisse, B.; Jumas, J. C.; Monconduit, L. TiSnSb a New Efficient Negative Electrode for Li-Ion Batteries: Mechanism Investigations by Operando-XRD and Mössbauer Techniques. *J. Mater. Chem.* **2011**, *21*, 10069.

(24) Wilhelm, H. A.; Marino, C.; Darwiche, A.;

Soudan, P.; Morcrette, M.; Monconduit, L.; Lestriez, B. Engineering Study on TiSnSb-Based Composite Negative Electrode for Li-Ion Batteries. *J. Power Sources* **2015**, *274*, 496–505.

(25) Wilhelm, H. A.; Marino, C.; Darwiche, A.; Monconduit, L.; Lestriez, B. Significant Electrochemical Performance Improvement of TiSnSb as Anode Material for Li-Ion Batteries with Composite Electrode Formulation and the Use of VC and FEC Electrolyte Additives. *Electrochem. commun.* **2012**, *24* (1), 89–92.

(26) Madec, L.; Gachot, G.; Coquil, G.; Martinez, H.; Monconduit, L. Toward Efficient Li-Ion Cells at High Temperatures: Example of TiSnSb Material. *J. Power Sources* **2018**, *391*, 51–58.

(27) Fehse, M.; Darwiche, A.; Sougrati, M. T.; Kelder, E. M.; Chadwick, A. V.; Alfredsson, M.; Monconduit, L.; Stievano, L. In-Depth Analysis of the Conversion Mechanism of TiSnSb vs Li by Operando Triple-Edge X-Ray Absorption Spectroscopy: A Chemometric Approach. *Chem. Mater.* **2017**, *29* (24), 10446–10454.

(28) Schuhrke, T.; Mändl, M.; Zweck, J.; Hoffmann, H. Investigation of Surface Amorphization of Silicon Wafers during Ion-Milling. *Ultramicroscopy* **1992**, *41* (4), 429–433.

(29) McCaffrey, J. P.; Phaneuf, M. W.; Madsen, L. D. Surface Damage Formation during Ion-Beam Thinning of Samples for Transmission Electron Microscopy. *Ultramicroscopy* **2001**, *87* (3), 97–104.

(30) Mitome, M. Ultrathin Specimen Preparation by a Low-Energy Ar-Ion Milling Method. *J. Electron Microsc. (Tokyo).* **2013**, *62* (2), 321–326.

(31) Ramadass, P.; Haran, B.; White, R.; Popov, B. N. Capacity Fade of Sony 18650 Cells Cycled at Elevated Temperatures: Part II. Capacity Fade Analysis. *J. Power Sources* **2002**, *112* (2), 614–620.

(32) Xia, J.; Ma, L.; Dahn, J. R. Improving the Long-Term Cycling Performance of Lithium-Ion Batteries at Elevated Temperature with Electrolyte Additives. *J. Power Sources* **2015**, *287*, 377–385.

(33) Sinha, N. N.; Marks, T. H.; Dahn, H. M.; Smith, A. J.; Burns, J. C.; Coyle, D. J.; Dahn, J. J.; Dahn, J. R. The Rate of Active Lithium Loss from a Soft Carbon Negative Electrode as a Function of Temperature, Time and Electrode Potential. *J. Electrochem. Soc.* **2012**, *159*, A1672–A1681.

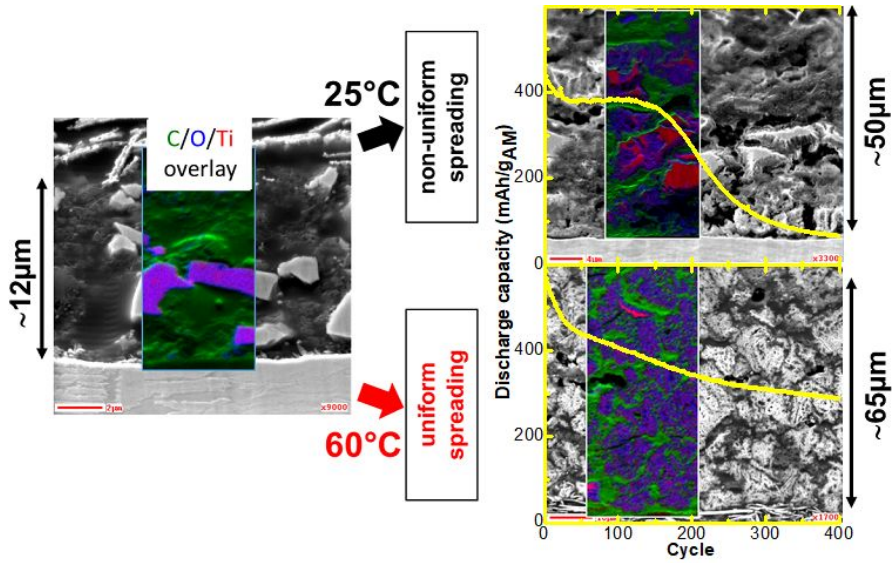
25°C
non-uniform spreading
C/O/Ti overlay
~12µm
60°C
uniform spreading
Discharge capacity (mAh/g$_{AM}$)
Cycle
~50µm
~65µm